Solar Energy Materials & Solar Cells 302 (2026) 114335

Contents lists available at ScienceDirect

Solar Energy Materials and Solar Cells

journal homepage: www.elsevier.com/locate/solmat

Improving V_{OC} in wide bandgap (Ag,Cu) (In,Ga)Se_2 solar cells for voltage-matched ACIGS/Si tandem modules

Ceren Mitmit [a,b,*], Matthias Diethelm [a], Matteo De Marzi [a], Nina Kochel [c], Joanna Maciejewska [c], Ajay Narasimhamurthy [c], Andrzej Miszczuk [c], Jessica de Wild [d,e,f], Bart Reekmans [d,e,f], Bart Vermang [d,e,f], Julia Horstmann [g], Romain Carron [a]

[a] Laboratory for Thin Films and Photovoltaics, Empa – Swiss Federal Laboratories for Materials Science and Technology, Überlandstrasse 129, 8600, Dübendorf, Switzerland
[b] Institute of Materials Science and Engineering, Ecole Polytechnique Fédérale de Lausanne (EPFL), Station 12, CH-1015, Lausanne, Switzerland
[c] Roltec Sp. z o. o., ul. Święty Marcin 29/8, 61-806, Poznań, Poland
[d] Hasselt University, Imo-imomec, Martelarenlaan 42, 3500, Hasselt, Belgium
[e] Imec, Imo-imomec, Thor Park 8320, Genk, 3600, Belgium
[f] EnergyVille, Imo-imomec, Thor Park 8320, 3600, Belgium
[g] Photovoltaics Group, Institute of Physics, Martin-Luther-University Halle-Wittenberg, Von-Danckelmann-Platz 3, 06120, Halle, Germany

ARTICLE INFO

Keywords:
(Ag,Cu) (In,Ga)Se_2
Cu(In,Ga)Se_2
Wide bandgap
V_{OC}
Voltage-matched tandem
Circuitry 2T

ABSTRACT

The open-circuit voltage (V_{OC}) deficit in wide-bandgap (Ag,Cu) (In,Ga)Se_2 (ACIGS) absorbers remains as the main limitation for their application in tandem solar cells. The roles of absorber growth temperature, surface treatment, and rubidium fluoride (RbF) post-deposition treatment (PDT) on the V_{OC} of wide-bandgap ACIGS solar cells on transparent substrates and their integration into voltage-matched two-terminal ACIGS/Si tandems are investigated. Growth below 415 °C leads to poor morphology, Cu deficiency at the rear contact, and diode non-idealities, whereas higher temperatures improve film quality and V_{OC}. An ammonia-based absorber rinsing step reduces V_{OC} at growth temperature 415 °C and low Rb doses, whereas DI-water rinsing better preserves V_{OC} and boosts short-circuit current density (J_{SC}). V_{OC}-loss analysis based on the photoluminescence quantum yield (PLQY) is used to separate absorber bulk and interface contributions which are challenging to distinguish in complete solar cells. Quasi-Fermi-level splitting and diffusion-length estimates reveal that non-radiative recombination dominates V_{OC}-loss, limiting the benefit of Ga back-grading.

Building on these insights, we present the first experimental demonstration of a voltage- and area-matched two-terminal bifacial ACIGS/Si tandem module, implementing a fully laser-interconnected top ACIGS sub-module. Voltage matching is achieved at 10 % rear illumination, with power density generation continuing to increase linearly beyond the voltage matching condition. In contrast to the more frequent series-connected tandems constrained by current matching conditions, the circuitry-2T architecture enables additional power gains under varying bifacial illumination.

1. Introduction

Chalcopyrite semiconductors offer a tunable bandgap, strong optical absorption, and long-term device stability. The Cu(In,Ga)Se_2 (CIGS) bandgap (E_g) can be tuned from ~1.0 to ~1.7 eV by adjusting the Ga/In ratio [1], enabling its use in both single-junction and in tandem solar cells. High efficiency CIGS devices have reached 23.6% [2] efficiency on molybdenum (Mo) and 19.8% [3] on transparent conductive oxide (TCO) back contacts. The combination of TCO as back contacts and high bandgap composition allow chalcopyrite devices to serve as wide-bandgap semi-transparent top cells. However, experimental demonstrations to date suffer from significant open-circuit voltage (V_{OC}) deficits due to limited absorber quality and rear-interface recombination [4,5]. These limitations are closely linked to the additional challenges associated with growth on TCO back contacts compared to conventional Mo substrates. The different substrate composition modifies alkali

* Corresponding author. Laboratory for Thin Films and Photovoltaics, Empa – Swiss Federal Laboratories for Materials Science and Technology, Überlandstrasse 129, 8600, Dübendorf, Switzerland.
E-mail address: ceren.mitmit@empa.ch (C. Mitmit).

https://doi.org/10.1016/j.solmat.2026.114335
Received 7 January 2026; Received in revised form 15 March 2026; Accepted 27 March 2026
Available online 4 April 2026

supply, requiring adapted alkali management during growth. In addition, the thermal process window is constrained by TCO stability, necessitating careful control of growth conditions [6,7].

Furthermore, in wide-bandgap CIGS obtained by increasing the Ga content, the resulting V_{OC} has consistently fallen short of expectations due to reduced grain size [8], higher density of deep defects such as Ga_{Cu}, Cu_{Ga} antisite [9,10], and stronger non-radiative recombination in the bulk and at interfaces [11,12]. High-Ga, wide-bandgap (wide-Eg) CIGS also shows larger exponential tail energies from enhanced subgap defect states and band tailing, further limiting V_{OC} [13,14]. CIGS on transparent back contacts (TBCs) such as ITO suffers from an additional V_{OC} penalty from modified interface properties [4]. Reported V_{OC} loss mitigation strategies include advanced co-evaporation (CuPRO(M) [15]), Ag alloying [16], alkali incorporation (Na, K, Rb, Cs) [17], and Ga back-grading [3,18–20]. Since Ag alloying has been reported to increase grain size [21], it is expected to be especially beneficial for high-Ga wide-bandgap absorbers that are prone to reduced grain size and higher recombination rate at the grain boundaries [22,23].

The co-evaporation substrate temperature critically affects crystal quality, elemental uniformity, and defects. Very high temperatures (>500 °C) improve crystallinity, interdiffusion, and grain growth in wide-E_g (GGI>0.6) [24–26] CIGS, whereas too low temperatures increase defects [27]. Yet high temperatures are not necessarily required for high-quality chalcopyrite; wide-Eg (Ag,Cu) (In,Ga)Se_2 (ACIGS) grown below 500 °C can remain highly crystalline - important for TCO-based devices with limited tolerance to thermal budget due to back contact stability and possible GaOx formation at the rear interface [6,7]. Ag alloying enables high-efficiency low-Eg ACIGS at 303 [21] – 353 °C [3], but process temperature limits for wide-E_g absorbers remain poorly explored.

RbF post-deposition treatment (PDT) improves performance via surface modification, grain-boundary passivation, and better band alignment [28,29], enabling thinner cadmium sulfide (CdS) with reduced absorption [18]. Absorber rinsing prior to CdS deposition removes contaminants and alkali residues; ammonia dissolves alkali compounds, removes In/Ga-rich phases, forms a Cu-Se layer, and eliminates oxides [30], but improper control can degrade the absorber-buffer interface [31,32].

Voltage-matched "circuitry-2T" tandem modules have been proposed to overcome the current-matching constraints of current-matched device, and improve the power output under changing illumination condition such as varying spectral distribution or bifacial operation [33,34]. Voltage matching can be achieved by adjusting the number of cells per submodule, allowing parallel connection without power electronics as the maximum power point voltage (V_{mpp}) varies only weakly with illumination. Voltage-matched 2T perovskite/Si [35] and GaInP/Si [36] modules have been demonstrated, but, to our knowledge, not CIGS/Si.

In this work, we fabricate wide-Eg ACIGS solar cells on ITO intended as top device in tandem photovoltaics. We analyze the V_{OC} losses by systematically investigating (i) Cu in-diffusion vs. temperature (bulk quality), (ii) absorber rinsing effects (interface properties), (iii) Rb incorporation (bulk & interface recombination), and (iv) Ga back-grading motivated by the need for wide-bandgap ACIGS top cell with reduced voltage losses for tandem applications. Through current-voltage (J-V) characteristics, external quantum efficiency (EQE), PLQY, scanning electron microscopy (SEM) imaging, secondary ion mass spectroscopy (SIMS) profiles, and temperature-dependent V_{OC} analyses, we establish correlations between processing parameters, recombination dynamics, and voltage losses. We then produce wide-E_g ACIGS minimodules on ITO and IO:H, optimize laser scribing, and integrate them with Si minimodules into voltage-matched circuitry-2T bifacial ACIGS/Si tandems, demonstrating stable voltage matching and the advantage of albedo gains under varying illumination from the rear side.

2. Methodology

This section reports the details of the fabrication and characterization of cells and mini-modules. The solar cell results reported in the next section were obtained with nine absorbers rinsed with both ammonia and water.

ACIGS cells fabrication: 12 nm Ag precursor layers were deposited by thermal evaporation onto commercially available SiO_x-barrier soda-lime glass coated with 200 nm of ITO (Kaivo, KV-ITO-P001). Then, CIGS absorbers were grown using a 3-stage co-evaporation process at nominal substrate temperatures 310 °C (1st stage), and 355, 415, or 455 (2nd and 3rd stage). Effective temperature values are believed slightly higher e.g. +40 °C. After the 3rd stage, an in-situ alkali post-treatment was applied at 305 °C nominal by sequential evaporation of NaF and RbF in Se ambient. The absorbers were completed by a 50 nm CdS buffer layer deposited by a chemical bath deposition technique. The transparent window consists of 70 nm intrinsic ZnO and 200 nm ZnO:Al (Al_2O_3 2 wt %) deposited by RF-sputtering. The devices were finished with electron beam evaporation of Ni (50 nm)/Al (4000 nm) grids and defined using mechanical scribing into 0.57 cm^2 cells.

Cells characterization: The integrated GGI and CGI ratios of the bare ACIGS absorbers were determined by XRF analysis using the Cu, Ga, and Se K-line intensities, calibrated against a set of reference samples. The I/III ratio was calculated from the XRF CGI value and the known Ag amount.

The current-voltage (J-V) measurements were obtained using a 4-contact scheme under standard test conditions (1000 Wm^{-2}, 25 °C) with a Keithley 2400 source meter under an ABA-class solar simulator replicating the AM 1.5G spectrum. EQE measurements were carried out using a Stanford Research Systems SR830 DSP lock-in amplifier in combination with a monochromator to spectrally resolve a halogen white light source. During the measurements, a halogen bias light of approximately 0.2 sun intensity was applied. The system was calibrated using calibrated Si reference cell. The bandgap Eg was extracted from EQE by following the PV bandgap calculation of Rau.

Absolute photoluminescence (PL) measurements were performed using a custom-built setup at room temperature (296 K). A chopped continuous wave 635 nm diode laser with a beam diameter of 1.6 mm was used for excitation, with photon flux calibrated to correspond to 1.7-sun illumination intensity (at 1.4 eV). Sample emission wavelength was set to 1.45 eV. The emitted PL signal was directed onto Ge photocell using a pair of 90° off-axis parabolic mirrors and spectrally filtered with a pair of longpass filters (cut-on wavelength: 700 nm).

Scanning electron microscopy (SEM) was performed using a Hitachi S-4800 microscope operated at an acceleration voltage of 5 kV.

V_{OC}-T measurements were acquired using Keithley source meter, with the samples placed in a temperature-controlled LN-cooled cryostat under a halogen light source with a set of neutral-density filters.

Compositional depth profiles were measured by ToF-SIMS on complete devices. The primary beam was 13 keV Bi^+ with a total current of 0.4 pA and a raster size of 100 × 100 μm^2. The sputtering beam was 600 nA, 2 keV O_2^+ with an on-sample area of 300 × 300 μm^2.

V_{OC} analysis: For a better understanding of the V_{OC}, the different voltage loss mechanisms are quantified following the approach of Rau et al. [37]. The solar cell V_{OC} is predicted according to Eq. (1).

$$V_{OC}^{pred} = V_{OC}^{SQ} - \Delta V_{OC}^{SC} - \Delta V_{OC}^{rad} - \Delta V_{OC}^{nonrad} \quad (1)$$

V_{OC}^{SQ} is the Shockley-Queisser limit voltage [38] of a single-junction solar cell with the PV bandgap E_g^{PV}. ΔV_{OC}^{SC} is the voltage loss due to a reduced J_{SC} as compared to its SQ value, ΔV_{OC}^{rad} is the radiative loss stemming from non-ideal absorption edge, and the non-radiative recombination losses ΔV_{OC}^{nonrad} are calculated from the PLQY measurement:

$$\Delta V_{OC}^{SC} = kT / q \ln\left(J_{SC}^{SQ} / J_{SC,measured}\right) \quad (2)$$

$$\Delta V_{OC}^{rad} = kT / q \ln\left(J_0^{rad} / J_0^{SQ}\right) \text{ where } J_0^{rad} > J_0^{SQ} \quad (3)$$

$$\Delta V_{OC}^{nonrad} = -kT / q \ln\left(J_0 / J_0^{rad}\right) \quad (4)$$

At open circuit, the external radiative efficiency (ERE ≈ PLQY) is given by $ERE = J_0^{rad}/J_0$

$$\Delta V_{OC}^{nonrad} = -kT/q \ln(PLQY) \quad (5)$$

The individual voltage loss terms ΔV_{OC}^{SC}, ΔV_{OC}^{rad}, and ΔV_{OC}^{nonrad} are defined following Rau et al., with value signs defined as positive. In particular ΔV_{OC}^{rad}, is expressed using the ratio of device to ideal radiative saturation currents J_0^{rad}/J_0^{SQ}) and ΔV_{OC}^{nonrad} uses the negative logarithm of the PLQY, consistent with Rau's sign conventions. Here J_0^{SQ} is the radiative recombination current density of an ideal SQ cell with the given bandgap. J_0^{rad} is the radiative recombination current of the actual device calculated by integrating the product of the measured external quantum efficiency Q_e^{PV} and the blackbody spectrum $\phi_{BB}(E)$. This calculation includes a geometrical factor $f_g = 2$ accounting for full spherical emission, following the method described by Rühle [39].

2.1. Mini-module fabrication and characterization

ACIGS mini-module fabrication: The fabrication of the ACIGS minimodule is based on the cells process described above. Four laser pattering processes were carried out between successive layer depositions, creating five individual cells connected in series. An Nd:YVO_4 pulsed picosecond laser was used for all processes. The first isolation scribe (P1) was carried out from the layer side (1064 nm wavelength, 3 W, 200 kHz repetition rate, 4 passes). The interconnection patterning process (P2) was performed after deposition of the absorber and buffer layers. To avoid damaging the rear contact, a mapping procedure was implemented to ensure constant working distance considering e.g. thickness variations in the CIGS absorber. The P2 structuring was performed with a laser power of 1.75 W and a repetition rate of 1 MHz, using three passes of the laser beam. The second isolation patterning process (P3) was performed after front TCO deposition.

Si mini-module fabrication: Si mini-modules were fabricated using shingling interconnection. The grid designs for the smaller cells were developed by imec, with finger printing performed by Meyer Burger. The 182 × 182 cm^2 Si cells provided by Meyer Burger were downsized into individual 0.9 × 4 cm^2 cells using a ps-pulsed laser. Five such cells were connected in series by shingling approach to obtain a module of 4 × 4 cm^2. A solar cell is first placed with the front side facing up. Small dots of electric conductive adhesive (ECA) are then applied to the busbar. Subsequently, another cell is placed busbar-to-busbar on the first solar cell, and these steps are repeated to assemble the complete module. This process is illustrated in Fig. S9. The top image (Fig. S9) shows a shingled cell with ECA applied to the busbar, while the bottom image shows a close-up of the adhesive droplets. Using a pick-and-place system, the shingled cells are positioned in a mold, as depicted in the left image. The overlap between cells is 1 mm. The ECA-bonded Si cells were sent to Sunplugged for further processing into a CIGS/Si voltage-matched module.

To determine the voltage at the maximum power point, fully encapsulated Si minimodules were also prepared. Current-voltage characterization was performed using a Loana and Wacom solar simulator under standard 1 sun condition, as well as under adapted spectra to simulate the transmitted light from the top module. Coated glass filters (5 × 5 cm^2) with long-pass wavelengths of 780 nm (1.6 eV) and 830 nm (1.5 eV) from Edmund Optics, in combination with a neutral density filter with 78 % transmission, were used to simulate the spectral transmission through the top cell. A special black absorbent sheet was applied to eliminate back reflection.

Tandem mini-module fabrication: Encapsulation was carried out using three ionomer lamination foils to provide mechanical stability and moisture protection. The external parallel connection of the ACIGS and Si minimodules was made using contact stripes.

Minimodule characterization: For bifacial J-V measurements, two Wavelabs Sinus-70 solar simulators were used simultaneously. A first solar simulator placed on top provided 1-sun, AM1.5 spectrum front illumination. A second solar simulator illuminates the sample from the rear though a glass plate, with AM1.5 spectrum distribution and tuneable intensity. The samples are illuminated during measurement for about 100 s, in order to prevent overheating of the cells in the absence of active sample cooling. No further cooling method was used. Measurements have not been compared with steady-state illumination.

Use of artificial intelligence: The authors used an artificial intelligence–based tool to assist with language editing and grammar refinement, and python coding for data visualisation. The AI tool did not generate scientific content, data, interpretations, or conclusions. All content was reviewed and verified by the authors, who take full responsibility for the manuscript.

3. Results and discussion

3.1. Parameters affecting V_{OC} in wide bandgap ACIGS solar cells

Nine ACIGS absorbers are reported, each of them cut in halves and rinsed with either water or ammonia before CdS buffer deposition. Table 1 summarizes the absorber parameters and photovoltaic (PV) performance of the corresponding solar cells. The values of absorber thickness, GGI, I/III and E_g were extracted as description in Section Methodology. The exponential tail decay energies were from the low energy portion of the EQE spectra (Fig. S1). Section 3.1 presents the results investigating successively the Cu in-diffusion vs. temperature, (ii) absorber rinsing effects, (iii) Rb incorporation, and (iv) Ga back-grading.

3.1.1. Absorber deposition temperature

The effect of substrate temperature on the absorber properties and device performance is first examined. Fig. 1a–d presents SEM cross-section images of absorbers deposited at nominal substrate temperatures 355 °C, 415 °C and 455 °C during the 2nd and 3rd stage of the 3-stage co-evaporation process. At 355 °C (Fig. 1a), a distinct layer is present near the back contact, composed of small and disordered grains. 415 °C (Fig. 1b) significantly improves the morphology, with a more compact and uniform grain structure. With 455 °C (Fig. 1d), large grains span the entire absorber thickness.

The SIMS depth profile (Fig. 1e) reveals significant deficiencies in both Cu and Ag near the back interface of the sample grown at 355 °C, matching the layer visible on the SEM images. It should be noted that the SIMS sputtering conditions lead to an apparent forward sputtering of the Cu. Furthermore, for this sample, the stoichiometry point was detected several minutes sooner than expected, and the final film I/III composition ratio was 0.81, considerably lower than the 0.90 value expected from the stoichiometry point detection. Besides, the J-V curve of the 355 °C device (Fig. 1f) exhibits a pronounced kink affecting the injection current. The layer at the rear of the sample grown at 355 °C is therefore considered as a so-called ordered vacancy compound (OVC), based on morphology, lower Cu and Ag content, and increased alkali amount (Fig. S2b). The severity of symptoms on J-V curve depend on sample specifics (OVC thickness, layer coverage, its composition and doping, band offsets presumed unfavorable [40]), yet are undesirable in the solar cells.

The kinetics of Cu in-diffusion impose a limit on the processing window related to the specifics of the 3-stage deposition process (Cu-poor → Cu-rich → Cu-poor). During the second stage, low deposition temperatures (<415 °C) slow down the Cu in-diffusion, so the top of the CIGS film reaches (over)stoichiometry segregating Cu-Se phases, while the bottom of the film remains Cu-poor. Therefore, the sample thermal emissivity changes before the whole film reaches stoichiometry, and the

Table 1
Process parameters and PV performance of best cells of the samples reported in this work. "W/A" indicates water rinsing or ammonia rinsing respectively. *Samples for which the XRF (X-ray fluorescence) I/III ratio deviated significantly from the value estimated from stoichiometry point detection (presence of an ordered vacancy compound, see text).

	Substrate temp. (°C)	NaF-PDT (min)	RbF-PDT (min)	Thickness (μm)	I/III	Eg (eV)	CBD CdS (min)	V_{OC} W/A (mV)	J_{SC} W/A (mA/cm^2)	FF W/A (%)	Efficiency W/A (%)	Exp decay (meV)
T355_Rb-H	355	20	20	2.28	0.81*	1.43	14	-/686	-/16.9	-/36.4	-/4.5	-/33
T355_Rb-H_1	355	20	20	2.21	0.83*	1.43	14	-/785	-/18.4	-/61.5	-/8.9	-/50
T355_Rb-H_2	355	20	20	2.28	0.79*	1.40	14	-/761	-/21.9	-/62.0	-/10.3	-/50
T415_Rb-H_1	415	20	20	2.00	0.89	1.44	14	-/835	-/16.0	-/52.4	-/7.0	-/30
T415_Rb-L	415	4	4	1.62	0.89	1.52	22	785/724	16.5/17.0	61.1/62.0	7.8/7.6	26/19
T415_Rb-H	415	4	16, +40 °C	1.57	0.91	1.51	22	871/824	14.4/14.9	54.4/50.7	6.8/6.2	24/28
T455_Rb-L	455	4	4	1.52	0.87	1.51	22	785/684	18.6/16.9	61.6/60.0	9.2/6.9	30/22
T455_Rb-H	455	4	16, +40 °C	1.54	0.90	1.52	22	874/875	17.7/18.0	65.1/60.5	10.1/9.5	29/29
T455_Rb-H_1	455	4	16, +40 °C	1.48	0.82	1.51	22	872/-	18.0/-	61.5/-	9.6/-	25/-

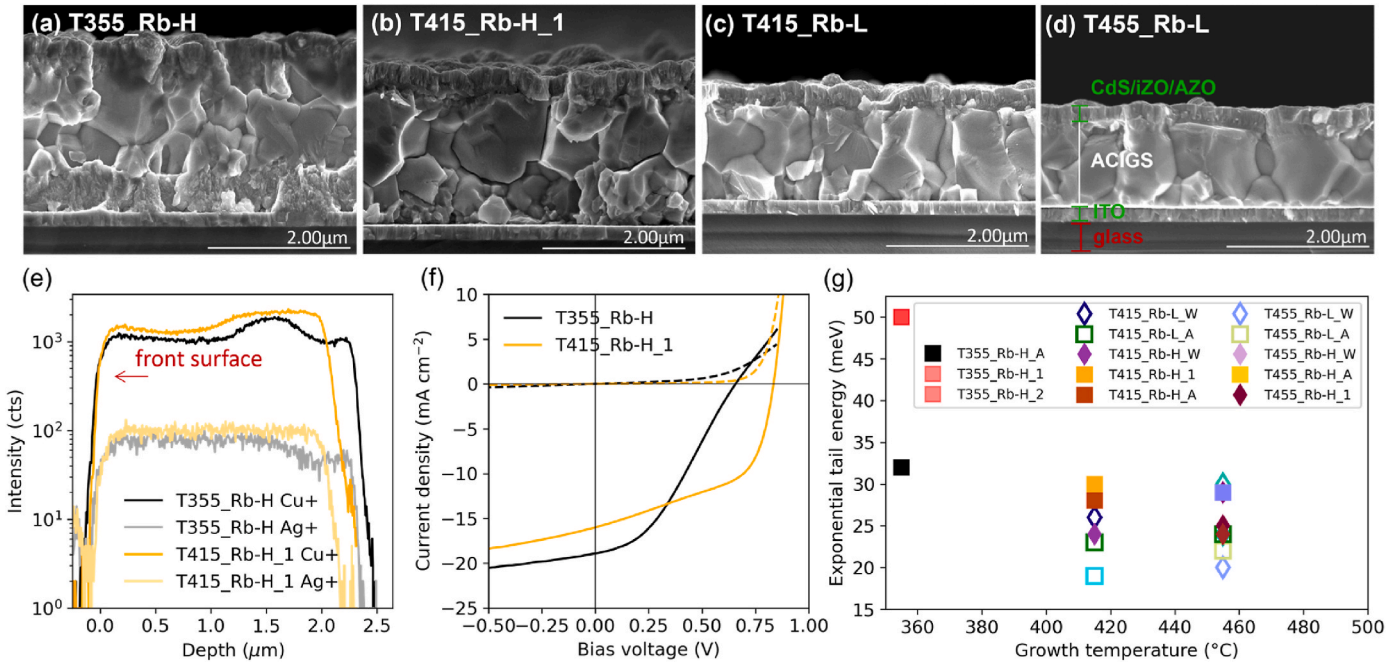

Fig. 1. (a-d) Cross-sectional SEM images of completed solar cells at different growth temperatures. (e) Tof-SIMS Cu+ and Ag + depth profile of samples grown at 355 and 415 °C., and (f) corresponding J-V curves. Through (a)-(f), all absorbers are ammonia-rinsed prior to buffer deposition. (g) Comparison of exponential decays from EQE measurements.

process control based on thermal signal is unreliable. This limit is specific to absorbers with high Ga contents, as even temperatures as low as 303 °C were found suitable for absorbers with low ~0.35 GGI ratio in the same deposition chamber [21].

The exponential EQE tail below the band edge (Fig. S1) indicates structural disorder in the absorber. Fig. 1g compares the extracted decay energies. T355_Rb-H shows the best decay value among all 355 °C samples, likely reflecting absorption in the chalcopyrite phase. The other two 355 °C samples show larger ~50 meV exponential decays. At 415 °C and 455 °C, the exponential tail energies are consistently smaller and more uniform than at 355 °C, implying improved crystallinity and reduced band tailing, though with notable variations between samples. No dependence on rinsing is seen. Increasing the Rb dose causes a modest ~9 meV increase and weaker at higher temperatures, although with unclear statistical significance. It is here assumed that the post-deposition treatments only marginally affect structural disorder and potential fluctuations.

3.1.2. *Absorber rinsing procedure*

After determining the minimum threshold for the absorber deposition temperature, the rinsing of bare absorbers prior to CdS deposition is investigated, comparing deionized (DI) water (10 min) and ammonia solution (3.7 M, 10 min). For comparison, the ammonia concentration in the CdS deposition bath is 2.1 M. Fig. 2a shows the J-V curves of the best cell of Rb-low samples at 415 and 455 °C, while Fig. 2b presents the corresponding cells V_{OC} distribution. The ammonia-treated samples exhibit a clear V_{OC} degradation, particularly at the higher deposition temperatures. The voltage reduction is accompanied by a blocking of

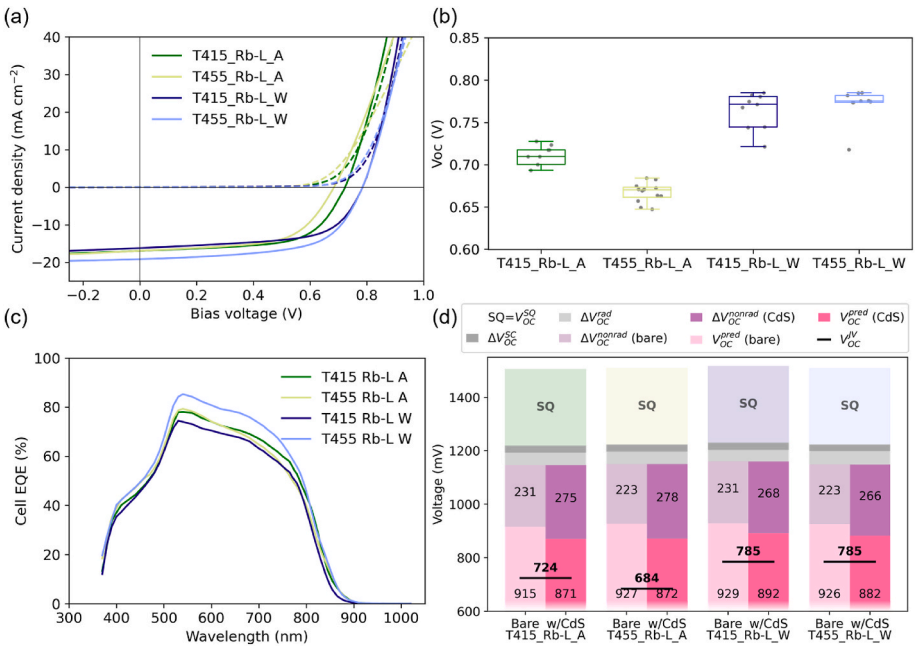

Fig. 2. (a) J-V measurement of best cells of samples with Rb-low absorbers rinsed with ammonia solution and DI water. (b) V_{OC} comparison of the cells on the same samples, and (c) EQE comparison of the best cells. (d) V_{OC} loss analysis of the corresponding samples discriminating the Shockley-Queisser limit ($\boldsymbol{V_{OC}^{SQ}}$) and the voltage loss terms arising from the measured J_{SC} being lower than SQ limit ($\Delta\boldsymbol{V_{OC}^{SC}}$), radiative recombination ($\Delta\boldsymbol{V_{OC}^{rad}}$), non-radiative recombination ($\Delta\boldsymbol{V_{OC}^{nonrad}}$).

diode current at high forward bias, particularly in the dark. As discussed in Ref. [31], this transport issue is attributed to interface modifications induced by the ammonia treatment altering the band alignment, the presence and nature of defects and/or interfacial compounds. In contrast, absorber rinsing with DI water results in better V_{OC} at both growth temperatures and yields the best J_{SC} at 455 °C.

The EQE spectra of the series (Fig. 2c) present similar shapes with wavelength, indicating that rinsing primarily affects the junction quality rather than bulk carrier collection. The slightly enhanced EQE for the DI-rinsed, high-temperature cells is consistent with their higher J_{SC}.

Fig. 2d presents a V_{OC} loss analysis of the rinsing series following Rau's approach [37] (see details in Section Methodology). PLQY were measured on bare absorbers as well as after rinsing and CdS deposition. The actual V_{OC} (V_{OC}^{JV}) is significantly below the predicted value V_{OC}^{pred}: the voltage losses are only partially evidenced by PLQY technique on buffer-covered absorbers. The water and ammonia rinsing treatments show comparable radiative losses (~43-50 mV). Yet the rinsing strongly affects the V_{OC}^{JV}: the DI-rinsed samples reach ~785 mV for both absorber

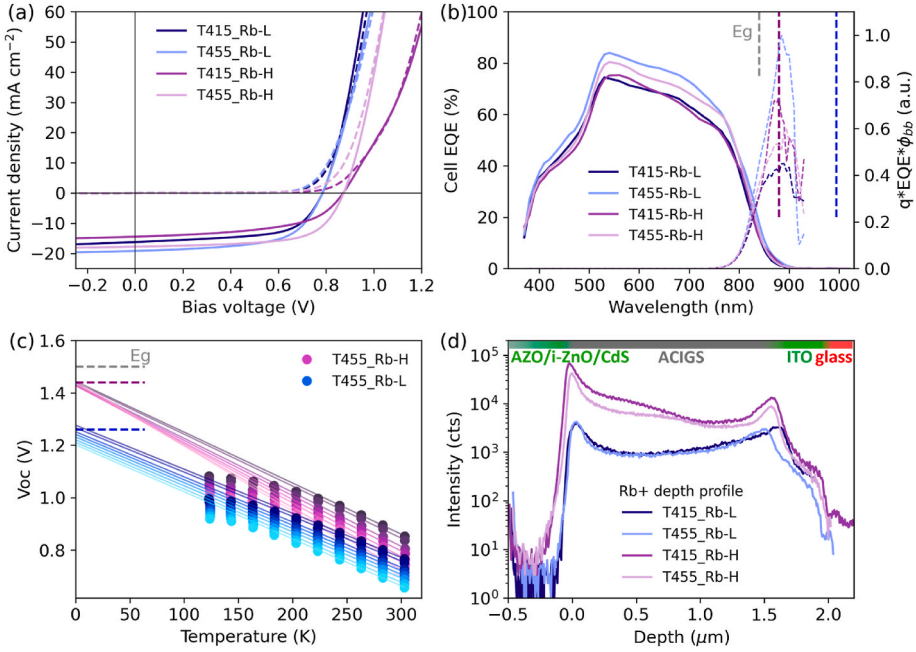

Fig. 3. (a) J-V measurement of best cells of samples, water-rinsed before buffer deposition. (b) Corresponding EQE measurements and their convolution with black-body spectrum as an approximation to the PL spectra. (c) V_{OC}-T measurement with highlighted activation energies as in panel (b). (d) ToF-SIMS Rb + depth profile of the same devices.

growth temperatures, whereas ammonia-rinsed ones drop to ~684 mV (455 °C sample). This ~100 mV difference is due for a small part to ΔV_{OC}^{nonrad} (~10 mV, see also Fig. S3), and more largely to an increased difference between the measured and predicted V_{OC}. It has been proposed that PLQY only partially reflects CdS/ACIGS interfacial recombination because the open-circuit band bending in CdS-terminated samples differs from that in full cells with high-resistivity layer (HRL) and TCO.

3.1.3. RbF post-deposition treatment

Here, devices treated with varying Rb content are compared to investigate voltage and charge recombination. Fig. 3a shows that a high dose of Rb significantly increases V_{OC}, independently of growth temperature. As the EQE shape at long wavelengths (Fig. 3b) is barely affected by the Rb dose indicating that bulk collection and crystallinity are not significantly altered. A consistent energy offset of nearly 100 meV between the optical bandgap (from the EQE derivative peak) and the convolution of the EQE with the black-body spectrum (approximating the PL spectrum; see Fig. 3b) is observed. This large shift suggests significant degree of electronic disorder, such as band tailing, that is not mitigated by larger Rb incorporation. Findings are further supported by temperature-dependent V_{OC} measurements in Fig. 3c. The high-Rb sample exhibits an activation energy (E_a) of ~1.42 eV consistent with absorber-dominated recombination (corresponds to the PL peak energy estimated from EQE convolution to blackbody spectrum). In contrast, the low-Rb device V_{OC}-T shows a significantly lower ~1.25 eV activation energy, suggesting an interface as the location of the dominant recombination, presumably at the buffer/absorber junction. This distinction highlights Rb's effectiveness in suppressing interface losses. In conclusion, Rb suppresses non-radiative recombination at or near the front interface.

Additionally, both V_{OC} and PLQY (see Fig. S3) are comparable for devices grown at 415 °C and 455 °C, indicating no strong temperature dependence within this range for the dominant recombination processes.

Although not affecting V_{OC}, higher absorber deposition temperatures increase J_{SC}, reflected by the overall upward shift in the EQE spectra without change in the spectral shape (Fig. 3b). The improvement in J_{SC} observed at higher growth temperatures likely stems from enhanced charge collection rather than morphological changes alone. This trend is consistent with our earlier findings [41], where interface-related effects, particularly variations in surface doping and junction barrier height, was found to limit the photocurrent collection in wide-bandgap ACIGS on TBCs. Higher processing temperatures may alleviate the postulated transport barriers by e.g. improving compositional uniformity or mitigating excessive doping near the front interface. In contrast, increasing the Rb content reduces J_{SC} by ~2 $mAcm^{-2}$. The statistical distribution of cells J_{SC} values is shown in Fig. S4.

SIMS depth profiling (Fig. 3d) shows buildups of Rb at both front and rear interfaces, while the Rb concentration in the bulk approaches saturation (increases comparatively less than the bulk). The high Rb concentration at the front interface might be connected to the slight blocking behaviour of sample T415_Rb-H, which was mitigated by increasing the temperature during second and third stages.

The influence of the I/III ratio on device performance is then investigated by comparing samples T455_Rb-H (I/III: 0.90) and T455_Rb-H_1 (I/III: 0.82). The different I/III ratios were obtained by adjusting the duration of the third stage in the three-stage co-evaporation process. No significant changes in device performance and good uniformity are observed within the I/III range of 0.82 to 0.90. The corresponding J-V and EQE data are provided in Fig. S6. By contrast, when I/III ratio exceeds 0.91, the V_{OC} collapses down to ~100-200 mV (see Fig. S5), due to the diode behaviour and not to shunting. These samples additionally exhibit a widespread in voltage (Fig. S5) due to the radial gradient in I/III ratio, several percent higher toward the corner: the corners show catastrophic V_{OC} values, while cells in the center of the sample may be well-performing.

Fig. 4 presents a detailed comparison of V_{OC} loss components for the devices listed in Table 1. The T355_Rb-H sample is excluded due to large subbandgap tail preventing reliable extraction of ΔV_{OC}^{rad} as the convolution of EQE and blackbody spectrum diverges at low energy. All samples present a substantial gap of at least 50 meV between the cell V_{OC}^{JV} (horizontal lines) and their predicted value (V_{OC}^{pred}, pink bars). This contrasts with the behaviour of Empa's low-bandgap ACIGS devices, for which the V_{OC} is very close to the corresponding in-house predictions. The V_{OC} of our wide-bandgap ACIGS devices is dominated by non-radiative recombination losses as shown in light and deep purple bars.

High Rb doses consistently improve V_{OC} and reduce the total V_{OC} deficit compared to their low-Rb counterparts. The improvement originates mainly from two factors: (i) a decrease in the ΔV_{OC}^{nonrad} determined from PLQY after CdS deposition (from >265 mV down to <225 mV), and (ii) a reduction in the difference between the predicted (V_{OC}^{pred}) and measured V_{OC} (V_{OC}^{JV}) from approximately 100 mV down to about 60 mV in the high-Rb devices. It is concluded that Rb incorporation mitigates interfacial recombination, likely through defect passivation or improved band alignment that limits the activity of defect states. Moreover, bare absorbers treated with high-Rb doses show a slightly reduced non-radiative recombination losses (from >220 mV down to ~210 mV), consistent with a slightly improved bulk quality or grain boundary passivation. Radiative losses (ΔV_{OC}^{rad}) remain mostly unchanged across samples at a relatively high level (40-50 mV) compared to low E_g ACIGS devices fabricated at Empa (20 mV): the Rb PDT treatment could not reduce the density of tail states affecting the EQE shape.

With a high Rb dose, the ammonia-rinsed cells exhibit a distinctly improved loss profile compared to their low-Rb counterparts presented in Fig. 2, as they maintain low non-radiative losses even after CdS deposition. The specific combination of higher 455 °C growth temperature and high Rb dose enabled ammonia-rinsed devices with same voltage and performance as the water counterpart.

3.1.4. Gradient and rear interface recombination

Compositional depth profiles (Fig. S2) show a wide GGI back-graded region, becoming progressively flatter at higher deposition temperature (ΔGGI from ~0.40 at 355 °C to ~0.25 at 415 °C, and to ~0.20 at 455 °C). This specific grading is then evaluated to determine whether it is sufficient to shield the minority carriers from recombination at the rear interface. If the diffusion length L_d is comparable to or shorter than the absorber thickness, then recombination rate at the rear interface falls below that of bulk recombination, relaxing the requirements on the GGI gradient to prevent rear interface recombination to occur. L_d is estimated using:

$$L_d = \sqrt{D \cdot \tau} \tag{6}$$

where the D is diffusion coefficient ($D = \mu kT/q$) and τ *is* the carrier lifetime. As compared to state-of-the-art CIGS, our absorber present a similar doping density in the low 1e16 cm^{-3} range (see Fig. S7), and PLQY intensity 2 order of magnitude lower (2-3e-4 versus >1.6% ERE [2]). Lifetime is therefore clearly lower than 10 ns. Combined with reported minority carrier mobilities in CIGS (10 to 40 $cm^2 V^{-1} s^{-1}$, see also large grains in Fig. 1d), L_d must be < 1 μm. As our absorber thickness is larger (1.5-2 μm), the rate of bulk recombination dominates rear interface recombination even in an ungraded absorber, therefore the shallow ΔGGI difference of about 0.2 is enough to bring the voltage loss associated to rear interface recombination to a negligible level. Yang et al., [20] demonstrated that only absorbers with long diffusion lengths beyond the absorber thickness require large back-grading (ΔGGI >0.4), whereas for L_d < 1 μm, small gradients (ΔGGI ≲ 0.2) are already sufficient. Our absorbers fall in this short-L_d regime; therefore, even the lowest observed ΔGGI ≈0.2 is adequate to suppress rear-interface

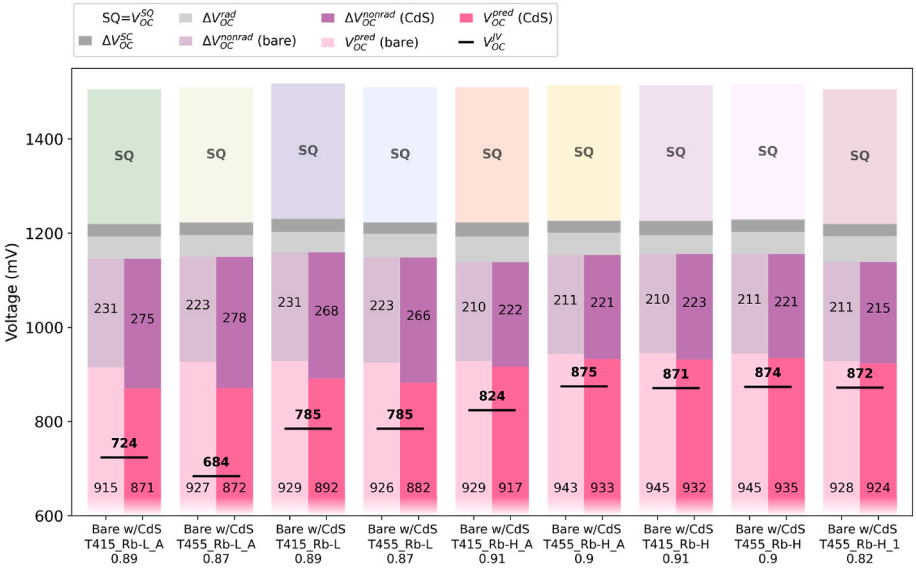

Fig. 4. V_{OC} loss analysis of the samples listed in Table 1. The I/III ratio is reported below the sample names. The letter "A" at the end of the sample names indicate samples are ammonia rinsed prior to buffer deposition.

recombination.

3.2. Application to tandem module demonstrators

3.2.1. ACIGS mini-modules

ACIGS mini-modules were manufactured by monolithically interconnecting 5 cells via laser patterning. Two mini-modules were processed on 5 × 5 cm^2 substrates, with 4 × 4 cm^2 central active area defined through P1 isolation scribes (details in Section Methodology). The mini-module with ITO back contact implemented a low-Rb absorber deposited at 415 °C motivated by the higher J_{SC} observed under these conditions. The mini-module with IO:H back contact featured a high-Rb absorber deposited at 455 °C to prioritize a higher V_{OC}. The laser fluence was optimized to fully remove the ACIGS layers inside the P2 scribe (interconnect trench) while leaving the TBC materials undamaged (see Fig. S8). Further, two approaches for the P3 isolation scribe were evaluated: by removing only the front TCO (P3_v1), or by removing the entire layer stack down to the bottom contact (P3_v2, see Fig. 5a). Despite numerous tests, the P3_v1 resulted in poor shunting resistance affecting the module V_{OC} and fill factor (FF) (Fig. 5b) due to insufficient electrical insulation of adjacent cells (Fig. 5b). Therefore, a second, adjacent P3_v2 structuring step was applied, improving shunt resistance and performance to 7.32 % efficiency, despite the slight widening of the dead area after reprocessing (around 260 µm).

Fig. 5b compares the I-V characteristics of mini-modules fabricated on ITO and IO:H [4,42]. For both minimodules the V_{OC} is comparable to that of corresponding cells, demonstrating successful processing of interconnections. The higher Rb content used in the IO:H-based mini--module resulted in a higher V_{OC} whereas the I_{SC} was reduced. Fig. 5c highlights the gain in transmittance achieved by using an IO:H back contact. With transmittance of ACIGS mini-module >70 %, the current density available in the bottom cell increases from 4.2 $mAcm^{-2}$ to 9.0 $mAcm^{-2}$ (based on the spectral response of a Meyer Burger Si cell).

3.2.2. Si mini-modules

Si mini-modules with an area of 4 × 4 cm^2 were prepared with an efficiency of approximately 18 % as described in Section Methodology. The losses from the 22 %-efficient base cells are attributed to downsizing and encapsulation, which mainly degrade V_{OC} and FF. For comparison, the cells cut to size presented about 19 % efficiency before stringing into mini-modules. Fig. 6b show the power curves of a Si mini-module under various illumination spectra using a neutral density (ND) filter (78 % transmission) and long-pass filters (780 nm and 830 nm). The V_{mpp} under these filters ranged between 2.55 and 2.65 V. The

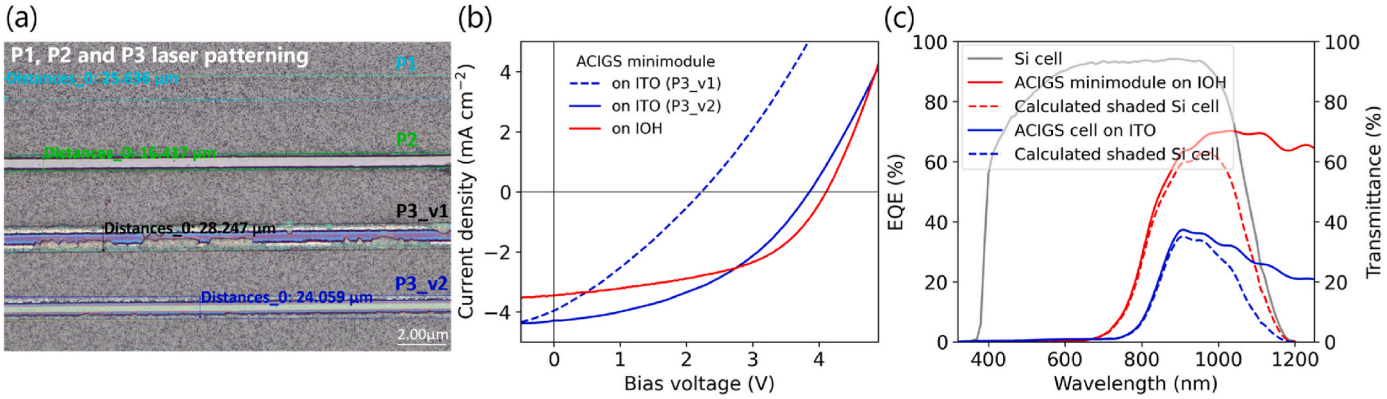

Fig. 5. (a) Optical microscope image of the re-scribed module overlayed with layout measurements. The laser steps P3_v1 patterns the top TCO, and the rescribed line P3_v2 cuts the layer stack down to the back contact. (b) I-V characteristics of the minimodules on ITO (7.1 % efficiency after P3_v2) and on IO:H (7.1 % efficiency). (c) Transmittance measurements of an ACIGS cell on ITO and minimodule on IO:H.

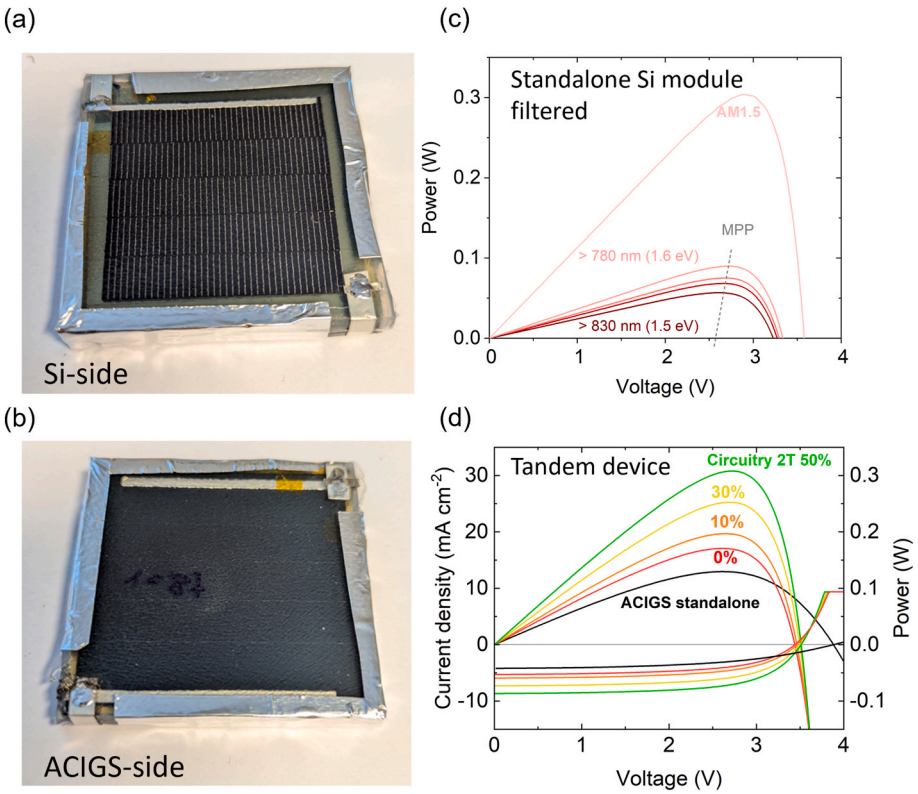

Fig. 6. (a) Top, Si-side and (b) rear ACIGS-side pictures of the tandem mini-module with ITO-based ACIGS submodule. (c) Performance of the Si mini-module under AM1.5 as well as filtered spectra to mimic reduced illumination below an ACIGS top device. The V_{MPP} reduces from 2.9 V to 2.55 V under combined 78 % ND filter and 830 nm long pass filter. (d) J-V and power-voltage curves of the ITO-based tandem minimodule with circuitry 2T configuration, with indicated back side illumination in percentage of AM1.5 standard photon flux. The black curves show the current density and power curves of the top ACIGS submodule measured before lamination.

number of cells in the design of the CIGS top modules was adapted to match the same value, satisfying the voltage matching condition.

3.2.3. 2T voltage-matched tandem mini-module

The previously described ACIGS mini-modules were stacked together with Si mini-modules, electrically connected in parallel, and encapsulated using standard technique (see the pictures of the tandem device in Fig. 6a and b). The 2T voltage-matched tandem module with ITO back contact yield an efficiency of 10.7 % with a designated aperture area of 4x4 cm^2. The tandem module with IO:H-based string presented a performance of 10.8 %, as the transparency gain into the bottom Si string was offset by the inferior ACIGS string performance (the device got unfortunately slightly shunted upon lamination). The V_{MPP} of the top and bottom strings of the ITO-based module are 2.62 V and 2.60 V, respectively. The V_{MPP} of the tandem is pinned close to the lower value, here the Si string at 2.60 V. The small 0.7 % voltage mismatch could be mitigated by bifacial operation: V_{MPP} voltage matching condition was achieved with 10 % albedo (additional illumination from the rear). Fig. 6d shows the power-generation density (PGD) of the tandem module, increased from 10.7 to 12.3 mW/cm^2 with 10 % rear illumination realizing voltage-matching. Beyond the voltage-matched condition, the PGD continues to increase, reaching 15.8 mW/cm^2 with 30 % rear illumination, and 19.25 mW/cm^2 with 50 % rear illumination (see Fig. S10). The observed gain in PGD originates from the increased current generation in the bottom module.

To analyze the behavior of the voltage-matched tandem device under mismatched illumination conditions, the PCE of the rear illumination component was calculated as the ratio of the gained output power to the additional rear-side illumination power, with 1-sun front side illumination as reference condition (see Fig. S10). The Si submodule operates almost optimally regardless of the rear illumination intensity (16.3-17.2 % PCE with rear illumination from 0.1 to 0.7-sun, versus about 18 % PCE standalone before encapsulation). For comparison, a current-matched tandem device subject to increased rear illumination beyond its current matching condition would barely produce any additional output power.

4. Conclusions

Our main findings are summarized as follows:

A minimum growth temperature is required: Wide bandgap ACIGS requires higher growth temperatures (≥415 °C nominal with the employed rates) than low bandgap absorbers. Reducing the temperatures (e.g. 355 °C) slows down Cu in-diffusion kinetics, leading to the presence Cu deficient OVC phases at the rear, degraded morphology and crystal quality (subbandgap tails), severely impacting voltage, FF (kinks in I-V curves) and solar cell performance.

Surface treatment matters: An ammonia-based rinsing before CdS deposition intended to remove excess alkali crystals degrades V_{OC}, while DI-water rinsing better preserves V_{OC} and improves J_{SC} on high temperature absorbers. The discrepancy reduced with absorber grown at high temperature and subject to high Rb dose. While outside the scope of this study, prior work at Empa on low-bandgap absorbers indicates that rinsing-induced voltage losses can depend on substrate specifics, which may also be relevant for wide-Eg absorbers. (e.g. opaque Mo vs TCO, glass composition etc.)

Rubidium PDT is the dominant lever for V_{OC}: High Rb incorporation enhances V_{OC} regardless of the growth temperature, which we attribute to reduced interface recombination with a minor trade off in J_{SC} and FF. A comparatively smaller improvement in internal voltage of bare absorbers is also evidenced: the PLQY measurements of buffer-covered absorbers does only very partially capture the interface

recombination voltage losses.

V_{OC} loss analysis highlights persistent ΔV_{OC}^{nonrad}: Decomposition of V_{OC} losses evidence similar contributions from radiative and short-circuit voltage loss across all devices, while the non-radiative recombination is the largest contributor to the V_{OC} deficit. While high Rb doses limit the voltage loss that is not captured by the V_{OC} prediction based on PLQY, further reduction of ΔV_{OC}^{nonrad} is essential to approach the theoretical V_{OC} and improve device efficiencies. First, the non-radiative recombination in the bulk can be tracked by PLQY measurements on bare absorbers (currently ~1e-4 range): improving the luminescence intensity should improve voltage, as well as J_{SC} and FF which are presumed also limited by the short diffusion length (<1 μm). Second, further improvement in the interface or buffer layer materials may close the gap to device V_{OC} to the internal absorber voltage caused by front interface recombination.

Voltage matched tandem minimodule: Fully laser-interconnected ACIGS minimodules were realized with efficiencies up to 7.1 %, using ITO and IO:H as back contacts. Both devices preserved the cell-level V_{OC}. An ITO-based mini-module was integrated together with a 18 % efficient Si mini-module into a circuitry 2T voltage-matched tandem device, achieving 10.7 % combined efficiency. The prototype achieves ideal voltage matching at ~10 % albedo, boosting the power output to 12.3 mW cm^{-2}. Yet the device accommodates considerably higher albedos, increasing power output to 15.7 mW cm^{-2} (30 % albedo) and 19.2 mW cm^{-2} (50% albedo). Throughout the entire albedo range from 0 % to 70 %, the device converts rear illumination into electricity with 16-17.5 % power conversion efficiency, very close to the standalone efficiency of the Si rear mini-module. The voltage matching configuration allows efficient conversion of light also in case of wide mismatch in the excitation intensities in the bottom and top devices (from approx. 0.25 under front illumination, to 1.3 with 70 % albedo).

Our work clarifies how growth temperature, surface treatment, and Rb post-deposition treatment govern V_{OC} and non-radiative recombination in wide-bandgap ACIGS solar cells. Among the investigated parameters, Rb incorporation is the most effective lever to improve V_{OC}, while sufficient growth temperature is a prerequisite for absorber quality. Surface treatment plays a secondary role related to interface. Voltage-loss and compositional analyses discriminate the respective importance of the recombination mechanisms in the bulk and at the interfaces. To further improve the bulk quality, absorber composition, absorber formation pathway and post-treatments strategies may be explored aiming at reducing the density of deep defects such as Ga_{Cu} and Cu_{Ga} antisite point defects, while the front interface recombination may be mitigated with a better tailoring of the front interface or with alternative buffer layers. The tandem results further confirm the excellent tolerance of the circuitry-2T configuration to variations in top and bottom illumination, supporting the suitability of wide-Eg ACIGS for tandem applications. While improving the performance of the Si submodule is largely a matter of upscaling, the largest achievable gains beyond the present tandem performance may be achieved by improving the efficiency of the wide-bandgap ACIGS solar cell material, mitigating the electrical losses at ACIGS subcells interconnections, and improving its optical transparency.

CRediT authorship contribution statement

Ceren Mitmit: Writing – review & editing, Writing – original draft, Validation, Software, Methodology, Investigation, Formal analysis, Conceptualization. **Matthias Diethelm:** Writing – review & editing, Validation, Methodology. **Matteo De Marzi:** Writing – review & editing, Validation, Methodology. **Nina Kochel:** Writing – review & editing, Methodology. **Joanna Maciejewska:** Methodology. **Ajay Narasimhamurthy:** Resources, Methodology. **Andrzej Miszczuk:** Writing – review & editing, Methodology. **Jessica de Wild:** Writing – review & editing, Visualization, Validation, Resources, Methodology. **Bart Reekmans:** Writing – review & editing, Methodology. **Bart Vermang:** Writing – review & editing, Methodology. **Julia Horstmann:** Writing – review & editing, Visualization, Resources, Methodology. **Romain Carron:** Writing – review & editing, Validation, Supervision, Resources, Project administration, Investigation, Funding acquisition, Conceptualization.

Declaration of competing interest

The authors declare that they have no known competing financial interests or personal relationships that could have appeared to influence the work reported in this paper.

Acknowledgements

This work has received funding from the Swiss State Secretariat for Education, Research and Innovation (SERI). Funded by the European Union. Views and opinions expressed are however those of the author(s) only and do not necessarily reflect those of the European Union or CINEA. Neither the European Union nor the granting authority can be held responsible for them. (HORIZON, project ID 101075626 "SITA", 101122203 "Hi-BITS"). This work has received funding from the Swiss National Science Foundation (SNSF) under grant no. 200021_197144/1 ("CIS"). Many thanks to Marcin Morawski for his suggestions and thorough revision of the article. Special thanks to to Dr Marek Basta for his support and sharing of versatile knowledge. The authors thank Raju Pusapati for providing Si pre-module fabricates to Sunplugged and Esin Aylin Melan for Si mini-module measurements. The authors thank Sunplugged for the minimodule encapsulation, and Meyer Burger (Germany) GmbH for their supply of Si cell with custom grids. Authors acknowledge the Laboratory for Surface Science & Coating Technologies at Empa for providing access to the SIMS facilities, and the Transport at Nanoscale Interfaces Laboratory at Empa for access to the SEM measurement infrastructure.

Appendix A. Supplementary data

Supplementary data to this article can be found online at https://doi.org/10.1016/j.solmat.2026.114335.

Data availability

Data will be made available on request.

References

[1] U. Rau, H.W. Schock, Cu(In,Ga)Se2 thin-film solar cells, in: T. Markvart, L. Castañer (Eds.), Pract. Handb. Photovolt., Elsevier Science, Amsterdam, 2003, pp. 367–413, https://doi.org/10.1016/B978-185617390-2/50016-7.

[2] J. Keller, K. Kiselman, O. Donzel-Gargand, N.M. Martin, M. Babucci, O. Lundberg, E. Wallin, L. Stolt, M. Edoff, High-concentration silver alloying and steep back-contact gallium grading enabling copper indium gallium selenide solar cell with 23.6% efficiency, Nat. Energy 2024 (2024) 1–12, https://doi.org/10.1038/s41560-024-01472-3.

[3] S.-C. Yang, T.-Y. Lin, M. Ochoa, H. Lai, R. Kothandaraman, F. Fu, A.N. Tiwari, R. Carron, Efficiency boost of bifacial Cu(In,Ga)Se2 thin-film solar cells for flexible and tandem applications with silver-assisted low-temperature process, Nat. Energy 8 (2022) 40–51, https://doi.org/10.1038/s41560-022-01157-9.

[4] J. Keller, L. Stolt, O. Donzel-Gargand, T. Kubart, M. Edoff, Wide-gap chalcopyrite solar cells with indium oxide–based transparent back contacts, Sol. RRL 6 (2022) 2200401, https://doi.org/10.1002/solr.202200401.

[5] J. Keller, N.S. Nilsson, A. Aijaz, L. Riekehr, T. Kubart, M. Edoff, T. Törndahl, Using hydrogen-doped In2O3 films as a transparent back contact in (Ag,Cu)(In,Ga)Se2 solar cells, Prog. Photovoltaics Res. Appl. 26 (2018) 159–170, https://doi.org/10.1002/PIP.2977.

[6] J.H. Choi, K. Kim, Y.-J. Eo, J.H. Park, J. Gwak, S.-K. Ahn, A. Cho, S. Ahn, J.-S. Cho, K. Shin, K. Yoon, S.H. Kong, J.-H. Yun, J. Yoo, Wide-bandgap CuGaSe2 thin film solar cell fabrication using ITO back contacts, Vacuum 120 (2015) 42–46, https://doi.org/10.1016/j.vacuum.2015.06.016.

[7] R. Gutzler, C.-Y. Song, D. Hariskos, H. Kempa, R. Scheer, R. Wuerz, E. Ahlswede, S. Paetel, W. Witte, Assessment of transparent conductive oxides as back contacts

for inline-fabricated Cu(In,Ga)Se2 solar cells, JPhys Energy 7 (2025) 045018, https://doi.org/10.1088/2515-7655/adfd86.
[8] S. Jung, S. Ahn, J.H. Yun, J. Gwak, D. Kim, K. Yoon, Effects of Ga contents on properties of CIGS thin films and solar cells fabricated by co-evaporation technique, Curr. Appl. Phys. 10 (2010) 990–996, https://doi.org/10.1016/j.cap.2009.11.082.
[9] S. Lany, Intrinsic DX centers in ternary chalcopyrite semiconductors, Phys. Rev. Lett. 100 (2008), https://doi.org/10.1103/PhysRevLett.100.016401.
[10] C. Spindler, F. Babbe, M.H. Wolter, F. Ehré, K. Santhosh, P. Hilgert, F. Werner, S. Siebentritt, Electronic defects in Cu(In,Ga)Se2: towards a comprehensive model, Phys. Rev. Mater. 3 (2019) 090302, https://doi.org/10.1103/PhysRevMaterials.3.090302.
[11] B. Huang, S. Chen, H.-X. Deng, L.-W. Wang, M.A. Contreras, R. Noufi, S.-H. Wei, Origin of reduced efficiency in Cu(In,Ga)Se_2 solar cells with high Ga concentration: alloy solubility versus intrinsic defects, IEEE J. Photovoltaics 4 (2014) 477–482, https://doi.org/10.1109/JPHOTOV.2013.2285617.
[12] A. Zunger, S.B. Zhang, S.-H. Wei, Revisiting the defect physics in CuInSe/sub 2/and CuGaSe/sub 2, in: Conf. Rec. Twenty Sixth IEEE Photovolt, Spec. Conf. -, 1997, 1997, pp. 313–318, https://doi.org/10.1109/PVSC.1997.654091.
[13] C.K.G. Kwok, N. Masuko, S. Ishizuka, R. Scheer, M.M. Islam, T. Sakurai, Recombination effects of urbach tails as trap states in Cu(In, Ga)Se2 solar cells probed by temperature-dependent junction-transient spectroscopies, Sol. RRL 9 (2025) 2400925, https://doi.org/10.1002/solr.202400925.
[14] F. Urbach, The long-wavelength edge of photographic sensitivity and of the electronic absorption of solids, Phys. Rev. 92 (1953) 1324, https://doi.org/10.1103/PhysRev.92.1324, 1324.
[15] P. Tsoulka, A. Rivalland, L. Arzel, N. Barreau, Improved CuGaSe2 absorber properties through a modified co-evaporation process, Thin Solid Films 709 (2020) 138224, https://doi.org/10.1016/j.tsf.2020.138224.
[16] J. Keller, K.V. Sopiha, O. Stolt, L. Stolt, C. Persson, J.J.S. Scragg, T. Törndahl, M. Edoff, Wide-gap (Ag,Cu)(In,Ga)Se2 solar cells with different buffer materials—A path to a better heterojunction, Prog. Photovoltaics Res. Appl. 28 (2020) 237–250, https://doi.org/10.1002/PIP.3232.
[17] N. Nicoara, R. Manaligod, P. Jackson, D. Hariskos, W. Witte, G. Sozzi, R. Menozzi, S. Sadewasser, Direct evidence for grain boundary passivation in Cu(In,Ga)Se2 solar cells through alkali-fluoride post-deposition treatments, Nat. Commun. 10 (2019) 3980, https://doi.org/10.1038/s41467-019-11996-y.
[18] R. Carron, S. Nishiwaki, T. Feurer, R. Hertwig, E. Avancini, J. Löckinger, S.-C. Yang, S. Buecheler, A.N. Tiwari, Advanced alkali treatments for high-efficiency Cu(In,Ga)Se $_2$ solar cells on flexible substrates, Adv. Energy Mater. 9 (2019) 1900408, https://doi.org/10.1002/aenm.201900408.
[19] M. Krause, S. Moser, C. Mitmit, S. Nishiwaki, A.N. Tiwari, R. Carron, Precise alkali supply during and after growth for high-performance low bandgap (Ag,Cu)InSe2 solar cells, Sol. RRL 8 (2024) 2400077, https://doi.org/10.1002/solr.202400077.
[20] S.C. Yang, M. Ochoa, R. Hertwig, A. Aribia, A.N. Tiwari, R. Carron, Influence of Ga back grading on voltage loss in low-temperature co-evaporated Cu(In,Ga)Se2 thin film solar cells, Prog. Photovoltaics Res. Appl. 29 (2021) 630–637, https://doi.org/10.1002/PIP.3413.
[21] S.-C. Yang, J. Sastre, M. Krause, X. Sun, R. Hertwig, M. Ochoa, A.N. Tiwari, R. Carron, Silver-promoted high-performance (Ag,Cu)(In,Ga)Se $_2$ thin-film solar cells grown at very low temperature, Sol. RRL 5 (2021) 2100108, https://doi.org/10.1002/solr.202100108.
[22] M. Gloeckler, J.R. Sites, W.K. Metzger, Grain-boundary recombination in Cu(In,Ga)Se2 solar cells, J. Appl. Phys. 98 (2005) 113704, https://doi.org/10.1063/1.2133906.
[23] M.A. Contreras, L.M. Mansfield, B. Egaas, J. Li, M. Romero, R. Noufi, E. Rudiger-Voigt, W. Mannstadt, Wide bandgap Cu(In,Ga)Se2 solar cells with improved energy conversion efficiency, Prog. Photovoltaics Res. Appl. 20 (2012) 843–850, https://doi.org/10.1002/pip.2244.
[24] J. Chantana, T. Watanabe, S. Teraji, K. Kawamura, T. Minemoto, Multi layer precursor method for Cu(In,Ga)Se2 solar cells fabricated on flexible substrates, Jpn. J. Appl. Phys. 53 (2014), https://doi.org/10.7567/JJAP.53.05FW03, 05FW03.
[25] S.V. Desarada, K.B. Chavan, S. Chaure, N.B. Chaure, Optimization of growth parameters of the RF-Sputtered CuInGaSe 2 thin films for photovoltaic applications, ECS J. Solid State Sci. Technol. 12 (2023) 085004, https://doi.org/10.1149/2162-8777/acedcf.
[26] H.L. Nguyen, H. Lee, S.F. Shaikh, H.A. Khan, M.S. Tamboli, J.H. Jung, N.T. N. Truong, Effects of growth temperature on the morphological, structural, and electrical properties of CIGS thin film for use in solar cell applications, Energies 16 (2023) 4467, https://doi.org/10.3390/en16114467.
[27] W. Li, L. Yao, K. Li, X. Li, B. Yang, S. Xu, S. Shi, C. Yi, M. Chen, Y. Feng, W. Li, Z. Lu, C. Yang, Enabling low-temperature deposition of high-efficiency CIGS solar cells with a modified three-stage Co-Evaporation process, ACS Appl. Energy Mater. 3 (2020) 4201–4207, https://doi.org/10.1021/acsaem.9b02025.
[28] P. Schöppe, S. Schönherr, P. Jackson, R. Wüerz, W. Wisniewski, M. Ritzer, M. Zapf, A. Johannes, C.S. Schnohr, C. Ronning, Overall distribution of rubidium in highly efficient Cu(In,Ga)Se_2 solar cells, ACS Appl. Mater. Amp Interf. 10 (2018), https://doi.org/10.1021/acsami.8b16040.
[29] E. Avancini, R. Carron, T.P. Weiss, C. Andres, M. Bürki, C. Schreiner, R. Figi, Y. E. Romanyuk, S. Buecheler, A.N. Tiwari, Effects of rubidium fluoride and potassium fluoride postdeposition treatments on Cu(In,Ga)Se2 thin films and solar cell performance, Chem. Mater. 29 (2017) 9695–9704, https://doi.org/10.1021/acs.chemmater.7b03412.
[30] C.L. Perkins, F.S. Hasoon, H.A. Al-Thani, S.E. Asher, P. Sheldon, XPS AND UPS investigation of NH/sub 4/OH-exposed Cu(In,Ga)Se/sub 2/thin films, in: Conf. Rec. Thirty-First IEEE Photovolt. Spec. Conf. 2005, 2005, pp. 255–258, https://doi.org/10.1109/PVSC.2005.1488117.
[31] I. Khatri, K. Shudo, J. Matsuura, M. Sugiyama, T. Nakada, Comparative study of water and ammonia rinsing processes of potassium fluoride-treated Cu(In,Ga)Se_2thin film solar cells, Jpn. J. Appl. Phys. 56 (2017), https://doi.org/10.7567/jjap.56.08mc12.
[32] R. Hertwig, S. Nishiwaki, M. Ochoa, S.-C. Yang, T. Feurer, E. Gilshtein, A.N. Tiwari, R. Carron, ALD-ZnMgO and absorber surface modifications to substitute CdS buffer layers in co-evaporated CIGSe solar cells, EPJ Photovolt. 11 (2020) 12, https://doi.org/10.1051/epjpv/2020010.
[33] J.M. Gee, A comparison of different module configurations for multi-band-gap solar cells, Sol. Cell. 24 (1988) 147–155, https://doi.org/10.1016/0379-6787(88)90044-0.
[34] M.H. Futscher, B. Ehrler, Efficiency limit of Perovskite/Si tandem solar cells, ACS Energy Lett. 1 (2016) 863–868, https://doi.org/10.1021/acsenergylett.6b00405.
[35] L.J. Geerligs, P. Manshanden, E. Hoek, L. Okel, I. Dogan, L. Simurka, H. Fledderus, V. Zardetto, D. Zhang, M. Najafi, A.E.A. Bracesco, M. Creatore, G.C. Coletti, S. C. Veenstra, Experimental investigation of 2-Terminal voltage-matched perovskite/crystalline silicon tandem modules, in: 2021 IEEE 48th Photovolt. Spec. Conf. PVSC, 2021, pp. 1553–1555, https://doi.org/10.1109/PVSC43889.2021.9518901.
[36] K. Alberi, J. Moore, K. Schmieder, M. Lumb, R. Walters, E. Armour, L. Mathew, R. Rao, Experimental demonstration of voltage-matched two-terminal tandem minimodules, J. Photon. Energy 8 (2018) 045504, https://doi.org/10.1117/1.JPE.8.045504.
[37] U. Rau, B. Blank, T.C.M. Müller, T. Kirchartz, Efficiency potential of photovoltaic materials and devices unveiled by detailed-balance analysis, Phys. Rev. Appl. 7 (2017) 044016, https://doi.org/10.1103/PhysRevApplied.7.044016.
[38] W. Shockley, H.J. Queisser, Detailed balance limit of efficiency of *p-n* junction solar cells, J. Appl. Phys. 32 (1961) 510–519, https://doi.org/10.1063/1.1736034.
[39] S. Rühle, Tabulated values of the shockley–Queisser limit for single junction solar cells, Sol. Energy 130 (2016) 139–147, https://doi.org/10.1016/j.solener.2016.02.015.
[40] M. Turcu, O. Pakma, U. Rau, Interdependence of absorber composition and recombination mechanism in Cu(In,Ga)(Se,S)2 heterojunction solar cells, Appl. Phys. Lett. 80 (2002) 2598–2600, https://doi.org/10.1063/1.1467621.
[41] M. Diethelm, C. Mitmit, C. Hägglund, M. Dimitrievska, W. Vels, S. Gharabeiki, Nisika, J. Keller, R. Carron, Enhancing photocurrent collection in wide-gap ACIGS solar cells, JPhys Energy 8 (2025) 015002, https://doi.org/10.1088/2515-7655/ae13c1.
[42] N. Nisika, S. Nishiwaki, C. Mitmit, M. De Marzi, R. Carron, High mobility and low carrier concentration transparent conducting oxide rear contact for bifacial CIGS solar cells, Prog. Photovoltaics Res. Appl. https://doi.org/10.1002/pip.70061.